IOP Publishing | International Atomic Energy Agency Nuclear Fusion

Nucl. Fusion **58** (2018) 036016 (16pp) https://doi.org/10.1088/1741-4326/aaa4d0

Plasma boundary shape control and real-time equilibrium reconstruction on NSTX-U

M.D. Boyer[1], D.J. Battaglia[1], D. Mueller[1], N. Eidietis[2], K. Erickson[1], J. Ferron[2], D.A. Gates[1], S. Gerhardt[1], R. Johnson[2], E. Kolemen[3], J. Menard[1], C.E. Myers[1], S.A. Sabbagh[4], F. Scotti[5] and P. Vail[3]

[1] Princeton Plasma Physics Laboratory, Princeton, NJ, United States of America
[2] General Atomics, San Diego, CA, United States of America
[3] Department of Mechanical and Aerospace Engineering, Princeton University, Princeton, NJ, United States of America
[4] Department of Applied Physics and Applied Mathematics, Columbia University, New York, NY, United States of America
[5] Lawrence Livermore National Laboratory, Livermore, CA, United States of America

E-mail: mboyer@pppl.gov

Received 6 September 2017, revised 22 November 2017
Accepted for publication 3 January 2018
Published 25 January 2018

Abstract

The upgrade to the National Spherical Torus eXperiment (NSTX-U) included two main improvements: a larger center-stack, enabling higher toroidal field and longer pulse duration, and the addition of three new tangentially aimed neutral beam sources, which increase available heating and current drive, and allow for flexibility in shaping power, torque, current, and particle deposition profiles. To best use these new capabilities and meet the high-performance operational goals of NSTX-U, major upgrades to the NSTX-U control system (NCS) hardware and software have been made. Several control algorithms, including those used for real-time equilibrium reconstruction and shape control, have been upgraded to improve and extend plasma control capabilities. As part of the commissioning phase of first plasma operations, the shape control system was tuned to control the boundary in both inner-wall limited and diverted discharges. It has been used to accurately track the requested evolution of the boundary (including the size of the inner gap between the plasma and central solenoid, which is a challenge for the ST configuration), X-point locations, and strike point locations, enabling repeatable discharge evolutions for scenario development and diagnostic commissioning.

Keywords: spherical torus, plasma boundary control, plasma boundary reconstruction, MIMO feedback control

(Some figures may appear in colour only in the online journal)

1. Introduction

The National Spherical Torus eXperiment Upgrade facility (NSTX-U) [1], which completed its first plasma operation campaign in 2016 [2, 3], aims to span between the previous class of spherical torus devices, like NSTX [4] or the mega-ampere spherical tokamak (MAST) [5], and future facilities planned to study plasma-material interaction [6], nuclear components [7], and demonstration of fusion power production [8, 9]. NSTX-U looks to build upon the results of NSTX [10] to improve the physics understanding of several key issues for future devices, including the scaling of electron transport with field and current [11–14], the physics of fast particles [15–18], and the achievement and sustainment of non-inductive, high-β scenarios [19–24]. One of the primary components of the upgrade project was the replacement of the 'center stack' (containing the inner-leg of the toroidal field (TF) coils, the Ohmic heating (OH) solenoid, and some divertor coils) with one capable of reaching much higher fields and providing more Ohmic flux for longer discharges.

The second major upgrade was the addition of a second neutral beam injector (NBI), aimed more tangentially, which significantly increases the auxiliary heating power and neutral beam current drive, and adds flexibility in shaping the spatial deposition of these quantities in the plasma. The upgrade increases the TF capability from 0.55 T to 1.0 T, the maximum plasma current from 1.3 MA to 2.0 MA, and enables full-field discharge durations of 5 s.

In order to take full advantage of the new device capabilities and to achieve the research goals of the NSTX-U program, real-time protection and control capabilities beyond those demonstrated on NSTX are required. In the area of device protection, a new digital coil protection system (DCPS) was implemented for NSTX-U that monitors the margins for current and temperature in each of the magnetic field coils along with the forces, moments, and stresses resulting from the combined effect of all coils [25, 26]. This system allows the operating envelope of the device to be expanded beyond the overly conservative limits imposed by a protection system based solely on individual coil current limits. In the area of plasma control, hardware upgrades along with a significant amount of algorithm design and software development were completed to update and improve legacy NSTX control algorithms, building upon the successful advances in control made during NSTX operation [27–30]. Furthermore, much progress has been made on the development of new algorithms for advanced control applications (e.g. [31–35]), including current and rotation profile, snowflake divertor control, and power/particle exhaust handling.

This paper focuses specifically on the NSTX-U plasma shape control system and results of its commissioning. Due to its importance for operations and scenario development, establishment of reliable feedback control of the plasma position and the shape of the plasma boundary was one of the first commissioning activities during initial plasma operations. By enabling accurate boundary control and repeatable discharge evolution, the system contributed to many milestones during the first NSTX-U campaign, including achieving scenarios of up to 1 MA, 0.65 T, and discharges with a 2 s pulse length [2, 3], as well as high beta discharges calculated to exceed the no-wall stability limit [36].

1.1. Organization

The paper is organized as follows: section 2 provides an overview of the NSTX-U coils and magnetic diagnostics, the control system hardware and software. The shape control approaches, requirements, and interactions with other algorithms are also described. In section 3, the gap control method used during the start-up and shutdown phases of discharges is described. Modifications to the real-time reconstruction code, which is used for more precise control of the plasma boundary, are described in section 4. In section 5, updates to the isoflux shape algorithm, which uses the results of the real-time reconstruction algorithm for precise plasma boundary control, are described. Results of controlling the outer gaps, X-point locations, strike point locations, vertical bias, and inner gap are presented. Conclusions and future work are discussed in section 6.

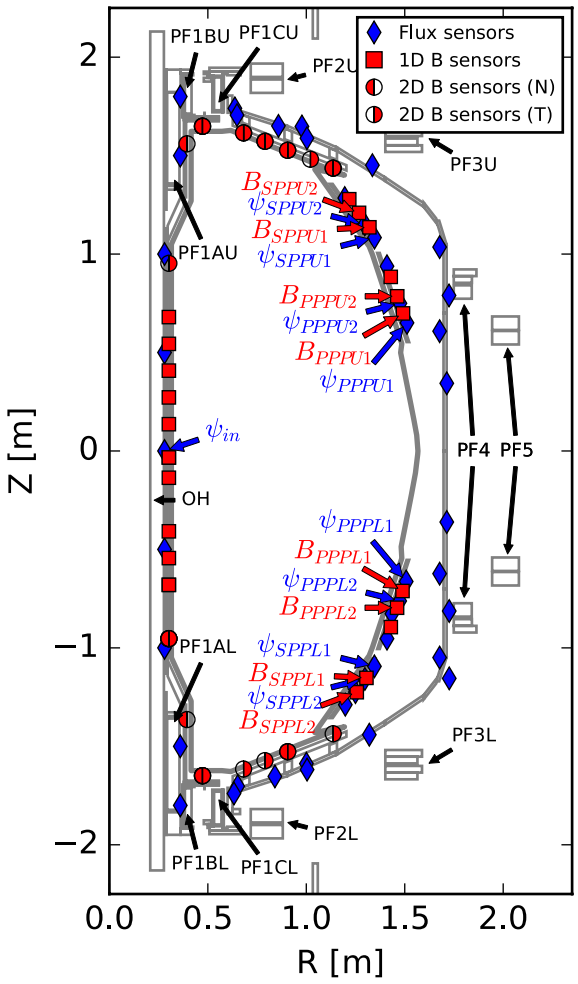

Figure 1. Poloidal cross-section of the NSTX-U poloidal field (PF) coils and vacuum vessel, along with the locations of flux loops (blue diamonds) and Mirnov coils (red squares and circles) used in the real-time magnetic control system. Red circles indicate '2D Mirnov coils', and are filled on the left side to indicate real-time use of the measurement of field normal to the tile the coil is installed in, on the right side to indicate use of the measurement tangent to the tile, or both sides to indicate use of both measurements. Specific flux and field measurements mentioned in other sections of the paper are also indicated.

2. Overview of shape control on NSTX-U

2.1. NSTX-U poloidal field coils

Figure 1 depicts a poloidal cross-section of the NSTX-U poloidal field (PF) coils and vacuum vessel, where the toroidal magnetic field is out of the page and the toroidal plasma current is into the page. The vertical field required to maintain a particular mid-plane outer gap (the distance between the plasma boundary and the outboard limiter) is primarily generated by the PF5 coil set, which consists of two coils wired in series, powered by a unipolar power supply. The PF4 coils, also wired in series, could be used to provide a portion of the vertical field, however, they were typically not used during

this campaign. The PF3U and PF3L are independently controlled with bi-polar power supplies, enabling their use for forming a poloidal field null at plasma breakdown, as well as for control of the plasma elongation, squareness, and vertical position. The PF2U, PF2L, PF1AU, and PF1AL divertor coils provide the field needed to form X-points in the divertor region, and are independently controlled with dedicated unipolar power supplies. The PF1B and PF1C coils sets were not used during this campaign, but will provide additional flexibility to vary the magnetic geometry of the divertor region in future campaigns. The OH coil is a solenoid designed for a maximum current of ± 24 kA that is used to inductively drive plasma current, while the toroidal field coils (twelve coils with three turns per coil, not shown) are designed to enable up to a 1 T magnetic field at $R = 0.936$ m.

2.2. NSTX-U poloidal field diagnostics

Also shown in figure 1 are the locations of the flux loops (blue diamonds) and Mirnov coils (red squares/circles) that provide flux and field measurements to the real-time system for use in estimating the position of the plasma boundary (either through estimates using a few sensors or through equilibrium reconstruction) and the vertical position of the plasma. Several of the installed field sensors are '2D Mirnov coils', which can provide measurements of the poloidal field in two perpendicular directions at each location. These are indicated by red circles. Some channels were not instrumented for real-time use or were found to be inoperable or unsuitably noisy: circles that are only half-filled indicate use of the measurement normal to the tile (left side filled) or tangent to the tile (right side filled). Fully filled circles indicate both channels were available for real-time use. Though channel availability varied slightly throughout the campaign, the diagnostics displayed in the figure represent the typically used diagnostic set of 44 flux loops and 52 Mirnov coils. The magnetic measurements were calibrated early in the campaign and are compensated in real-time for offsets, integrator drifts, and pick-up of stray 3D fields (e.g. fields from coil leads). The compensation for 3D fields was determined through a series of single coil vacuum test shots. These real-time measurements represent a subset of those used in offline equilibrium reconstruction, though most of the measurements used offline were available in real-time. Those measurements that are specifically mentioned in later sections are also labeled in the figure. Not pictured is a pair of Rogowski coils used to provide measurement of the plasma current, each of which are corrected for current in the vacuum vessel and four PF coils (PF1BU, PF1CU, PF1BL, and PF1CL) linked by the Rogowski coils. A more detailed description of these and other magnetic diagnostics on NSTX-U is found in [37].

2.3. NSTX-U control system

The NSTX-U control system (NCS) [38, 39], which includes the real-time hardware, protection systems, and software, acquires measurements from hundreds of diagnostic channels (including the magnetics described above) at a rate of 5 kHz using a set of custom-built stand-alone digitizers. Using the front panel data port (FPDP) protocol (ANSI/VITA 17.1-2003), these measurements are multiplexed onto a single serial data stream and communicated between the test cell and the real-time control computer over fiber. The real-time control computer runs the flexible plasma control system (PCS) software platform provided by General Atomics [40, 41], which allows customized categories of control algorithms to be developed within a powerful real-time control infrastructure. As part of the upgrade, many improvements to the NCS hardware have been made to increase the computational power available for the PCS, reduce latency, and expand the number of diagnostics and actuators under real-time control [38]. In particular, a new real-time control computer was installed with 64 2.8 GHz cores and a real-time kernel, and compiler tools for the PCS software were upgraded to take advantage of the newer hardware. Commands from the real-time computer are sent over fiber to FPDP output modules (FOM) dedicated to each actuator. In the case of the shape control algorithms, voltage commands are translated to firing angles and sent to output modules for the thyristor rectifier power supplies associated with each coil set. These commands are then locally translated to the required thyristor pulses.

2.4. Plasma shape control system roles and requirements

The primary role of the plasma shape control system is to establish the position and radial/vertical extent of the plasma, as well as its configuration (limited on a plasma facing component (PFC), or diverted with one or two X-points defining the plasma boundary). Control of the plasma boundary is critical for avoiding undesired wall-interaction (i.e. maintaining specified gaps between the plasma and PFCs) and for establishing plasma stability and evolution. For example, in [31, 35], simulations with the integrated modeling code TRANSP showed that modifying the plasma shaping can be used as a virtual actuator to actively control the current profile in NSTX-U by affecting bootstrap current and beam current drive profiles.

Furthermore, due to NSTX-U's large available heating power, high performance shots planned for future campaigns could potentially challenge the heat load handling capability of the PFCs. Local heating can be actively controlled through sweeping the location of strike points while heat load sharing between the top and bottom divertors can be controlled through actively maintaining balanced double null, or lower-/upper-biased discharges. This biasing is typically achieved through feedback control of the parameter δr_{sep}, defined as the horizontal distance between the two flux surfaces passing through the upper and lower X-points as measured at the outboard midplane plasma boundary. This parameter, along with the radial position of the X-points relative to the geometric center of the plasma, were also observed to influence the heating power required to induce the L–H transitions [42–44]. Therefore, active control of X-point positions and δr_{sep} enables optimization of the discharge shaping for triggering L–H transition. Reliably realizing L–H transition early in discharges when

neutral beam absorption is low is critical for developing high-performance H-mode discharges on NSTX-U [3].

The shape control system must also respond to disturbances due to changes in plasma conditions, e.g. changes in pressure due to confinement improvement/degradation. A closed loop response time of a few tens of milliseconds and tracking gaps or X-point/strike point locations to within a centimeter or two is typically suitable for scenario development purposes, however future applications, like strike point sweeping for heat flux management, may motivate future efforts to tune the control system to meet more stringent requirements, like faster response and/or better disturbance attenuation.

2.5. Overview of plasma shape control approaches

Two main shape control approaches are used on NSTX-U: the 'gap control' algorithm and the 'isoflux' control algorithm.

The gap control algorithm is used to control the PF coil voltages to either track a coil current target ('current control' mode) or to control the plasma outer gap and elongation based on estimates of these quantities from a small set of flux loop and field measurements ('gap control' mode). The latter capability is intended to provide approximate control of the plasma position during the early and end parts of discharges when the plasma current is not large enough for the plasma equilibrium to be reliably reconstructed in real-time. Details of this algorithm and results from commissioning are described in section 3.

To enable more precise control of the plasma shape during the main part of the discharge, a realistic solution to the plasma force balance can be calculated in real-time, provided the plasma current is suitably large to obtain reliable reconstructions. The rtEFIT algorithm [45] was used for real-time equilibrium reconstruction for several years on NSTX, beginning in 2003 [27], and several updates applied for use in NSTX-U are described in section 4. Based on the real-time equilibrium reconstructions calculated by rtEFIT, the isoflux control algorithm [45, 46] compares the flux at a set of target locations, referred to as control points and defined by the intersection of the operator programmed target boundary shape with a set of control segments. Through feedback modification of the voltage applied to the PF coils, these fluxes are made to match a reference flux, which may be defined by the flux at a limiter touch point or an X-point depending on the plasma configuration. In the case of diverted discharges, the isoflux control algorithm also enables precise control of X-point and/or strike point locations. To reduce computation time, the X-points, if present, are identified in real-time within two specified regions called control grids. Figure 2 shows the control segments, grids, and points for a typical diverted discharge. Updates to the isoflux algorithm and results of commissioning are described in section 5.

2.6. Interactions with other algorithms and algorithm sequence

The shape control system must interact with several other control algorithms, primarily the fast vertical controller and the plasma current controller.

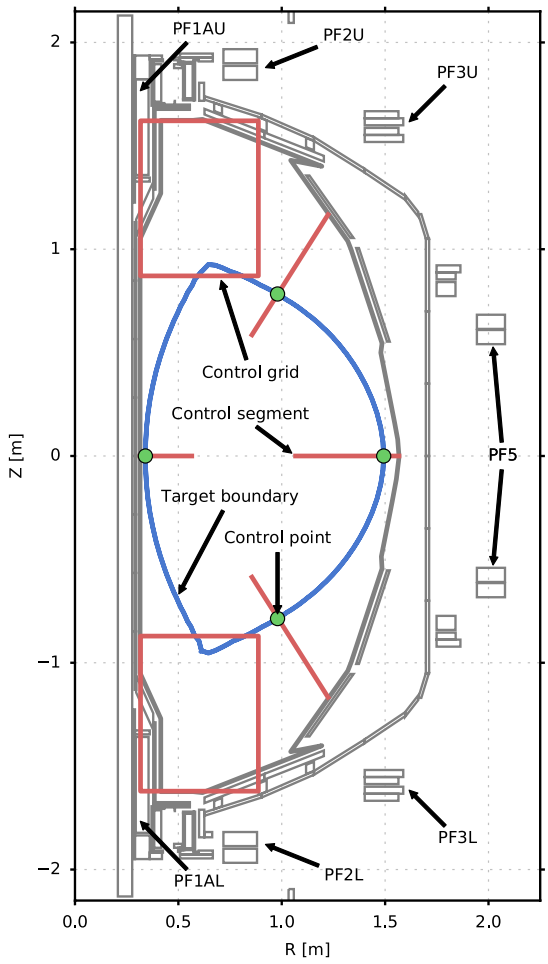

Figure 2. Control segments and grids used in the isoflux algorithms, showing the control points that are controlled during a typical diverted L-mode discharge.

The vertical control algorithm derives PF3U/L voltage requests based on a proportional-derivative control law acting on the plasma current weighted vertical position, estimated as:

$$I_p Z_p = \sum_i \alpha_i (\psi_{U,i} - \psi_{L,i}) \quad (1)$$

where α_i is the weight on the ith pair of otherwise identical flux loops located above and below the mid-plane, with flux measurements denoted $\psi_{U,i}$ and $\psi_{L,i}$ [37]. To reduce noise, the derivative term in the vertical control algorithm is not calculated from a numerical derivative of (1), but rather by a weighted sum of the measured difference in voltage between each pair of flux loops using the same weights as in (1). The voltage request from the vertical control algorithm is added to the voltage request from shape control algorithms.

The plasma current control algorithm adjusts the voltage on the OH coil in response to differences between the requested plasma current and the current measured by the Rogowski coils. While the OH coil is not used by either of the shape control algorithms, the fringing field of the OH coil affects the plasma shape and evolves as the OH coil current ramps throughout the pulse to induce plasma current. Furthermore, the OH coil current ramp induces currents in the conducting structures of the

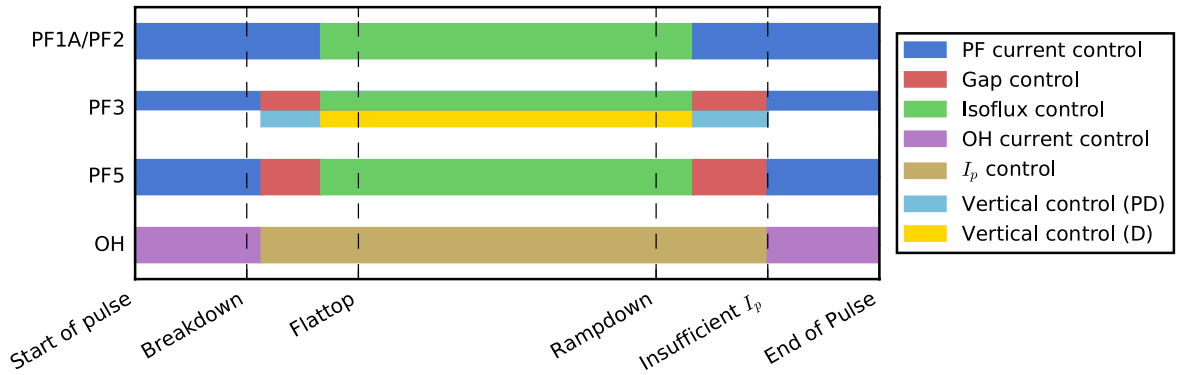

Figure 3. Timeline of a typical NSTX-U discharge showing algorithms associated with each coil set during the major phases of the discharge.

vacuum vessel, especially early in the pulse when loop voltage is high. These currents affect the plasma equilibrium, and can, at least early in the pulse, be large compared to the plasma current.

Figure 3 depicts a timeline of a typical NSTX-U discharge illustrating the various algorithms associated with each coil set during the major phases of the discharges. In a typical discharge, all of the PF coils begin in 'current control' mode to form the null for breakdown and to then form the plasma confining field. The OH coil current is programmed to ramp down in order to provide loop voltage required to initiate and ramp up the plasma current. Around 20 ms after plasma initiation, the OH coil is assigned to feedback control the plasma current, the proportional-derivative vertical control algorithm is activated, and the PF3 and PF5 coil sets enter 'gap control' mode to control the outer gap and elongation of the plasma. The divertor coils remain in 'current control' mode to, if required for the scenario, form upper and lower X-points. Once the plasma current ramps to a suitably large value (≈300 kA), the PF coils are switched to the isoflux algorithm to provide precise feedback control of the control points and, if required for the scenario, X-point and/or strike point locations. When using the isoflux algorithm, the vertical position is indirectly controlled by the position of the upper/lower outer boundary points and the X-point locations, so the proportional gain in the fast vertical control algorithm is typically set to zero and the vertical control algorithm only provides stabilizing derivative control. After the flattop phase of the discharge, once the plasma current drops below the threshold for reliable real-time equilibrium reconstruction, the divertor coils are returned to 'current control' mode, the PF3 and PF5 coil sets to the 'gap control' mode, and the proportional term in the vertical control algorithm is reactivated. When the plasma current drops to nearly zero, all of the coils are returned to 'current control' mode to return the coil currents to zero.

3. Coil current and boundary gap control algorithm

This section details the calculations and results of using the gap control algorithm, which enables each PF coil to be configured for one of two modes: 'current control' mode, in which voltages are calculated to track an operator programmed coil current, or 'gap control' mode, in which the coil voltage is determined based on feedback on an approximation of the mid-plane outer gap and elongation calculated from a small set of flux loop and field measurements. While a similar gap control approach was used on NSTX for controlling the mid-plane outer gap, the new version has been updated to include feedback control of the plasma elongation through the PF3 coils, which were only used in 'current control' mode on NSTX. This is an important new feature for maintaining good control of the plasma shape when ramping up using different initial Ohmic coil currents or when using the algorithm during plasma ramp-down once the plasma current drops too low for reliable real-time reconstruction.

3.1. Real-time algorithm calculations

For those coils selected to be under 'current control', the target current is calculated as

$$I_{\text{target}} = C_{\text{PF}} I_{\text{P,LP}} + f_{\text{PF}} I_{\text{OH,LP}} + I_{\text{PF,offset}} \tag{2}$$

where C_{PF} is a proportionality constant to the low-pass filtered measurement of the plasma current $I_{\text{P,LP}}$, f_{PF} is a proportionality constant to the low-pass filtered measurement of the Ohmic coil current, $I_{\text{OH,LP}}$, and $I_{\text{PF,offset}}$ is the operator programmed current target offset. The proportionality constants are used, for example, to maintain approximately fixed X-point positions by scaling the divertor coil currents with the plasma current, or to reject the effects of the Ohmic coil fringing field. Appropriate values of C_{PF} and f_{PF} were determined by scanning a target range of I_{OH}, I_{P}, β_N, l_i, κ, and other shaping parameters in a free boundary equilibrium code. A proportional-integral-derivative (PID) controller is used to modify the voltage requests for each coil to track its target current.

For those coils that are configured for use in 'gap control' mode (PF3U/L and PF5) their voltage request is determined based on two flux errors: one a proxy for the mid-plane outer gap, the other a proxy for the plasma elongation. The flux error for the outer gap, $E_{\text{gap,out}}$ is calculated as

$$E_{\text{gap,out}} = \psi_{\text{outp}} - \psi_{\text{in}} - \left(\frac{\partial \psi_{\text{outp}}}{\partial R} \cdot g_{\text{out}}\right), \tag{3}$$

where ψ_{in} is an inboard flux measurement, ψ_{outp} is an outboard flux measurement, $\frac{\partial \psi_{\text{outp}}}{\partial R}$ is the radial gradient of the outboard flux measurement, and g_{out} is the desired gap between the

outboard flux measurement and the plasma edge. The inboard flux measurement, $\psi_{\rm in}$, is provided by a single flux loop circling the center stack near the mid-plane and is indicated in figure 1. The flux $\psi_{\rm outp}$ is formed by weighting the flux measurements from pairs of up-down symmetric flux loops on the primary passive plates, i.e.

$$\psi_{\rm outp} = \sum_{i=1}^{3} \left[\beta_i \left(\psi_{\rm PPPU,\mathit{i}} + \psi_{\rm PPPL,\mathit{i}}\right)/2\right] / \sum_{i=1}^{3} \beta_i, \qquad (4)$$

where β_i is the weight on the ith flux loop pair. The flux loops used in typical NSTX-U discharges are indicated in figure 1. The radial derivative $\frac{\partial \psi_{\rm outp}}{\partial R}$ is calculated using up-down symmetric Mirnov coils positioned close to each flux loop:

$$\frac{\partial \psi_{\rm outp}}{\partial R} = \sum_{i=1}^{3} \left[\beta_i \pi R_{\rm sensor,\mathit{i}} \left(B_{\rm PPPU,\mathit{i}} + B_{\rm PPPL,\mathit{i}}\right)\right] / \sum_{i=1}^{3} \beta_i, \quad (5)$$

where $R_{\rm sensor,\mathit{i}}$ is the radial position of the ith sensor pair. The Mirnov coils measure both radial and vertical components of the magnetic field, thus equation (5) assumes the poloidal field is up–down symmetric such that the sum of the sensor signals isolates the vertical component of the field. The Mirnov coils used in typical NSTX-U discharges are indicated in figure 1.

A second flux error, $E_{\rm gap,sp}$, is calculated as

$$E_{\rm gap,sp} = \psi_{\rm outp} - \psi_{\rm outs} - \left(\frac{\partial \psi_{\rm outp}}{\partial R} g_{\rm sp}\right). \qquad (6)$$

The flux $\psi_{\rm outs}$ is formed by weighting the flux measurements from pairs of up-down symmetric flux loops on the secondary passive plates, i.e.

$$\psi_{\rm outs} = \sum_{i=1}^{3} \left[\epsilon_i \left(\psi_{\rm SPPU,\mathit{i}} + \psi_{\rm SPPL,\mathit{i}}\right)/2\right] / \sum_{i=1}^{3} \epsilon_i, \qquad (7)$$

where ϵ_i is the weight on the ith sensor pair. The secondary gap, $g_{\rm sp}$, is the desired radial distance between the flux surface passing through the primary passive plate sensors and the one passing through the secondary passive plate sensors, as measured at the location of primary passive plate sensors. This gap serves as a proxy for the curvature of the flux surfaces around the passive plates. A more positive value makes the flux surfaces more elongated.

Once calculated, the flux errors are converted to coil current errors using the gain matrix $M_{\rm G}$, i.e.

$$\begin{bmatrix} E_{\rm PF5} \\ E_{\rm PF3} \end{bmatrix} = M_{\rm G} \begin{bmatrix} E_{\rm gap,out} \\ E_{\rm gap,sp} \end{bmatrix}. \qquad (8)$$

This matrix enables multiple coils to be assigned to each controlled gap, however, in practice, it was found to be suitable to choose the off-diagonal elements of this matrix to be zero. The diagonal elements were chosen based on the expected change in the outer and secondary gaps in response to a change in the PF5 and PF3 currents, respectively. Finally, a PID control algorithm is used to adjust the voltage requests for each coil to drive this calculated current error to zero.

3.2. Experimental results

An example of the performance of this algorithm for a diverted L-mode discharge with 1MW NBI heating produced early in NSTX-U operations prior to commissioning real-time equilibrium reconstruction based shape control is shown in figure 4. In this shot, PF1A was the only divertor coil pair used, and was controlled using the relational scheme from (2). The inboard and secondary flux surfaces (dashed-lines), along with the plasma boundary (solid lines) are shown in figure 4(*a*) for $t = 0.4$ s (start-of-flattop) and $t = 1.0$ s (end-of-flattop). The average radial positions of intersections of the the inboard and secondary flux surfaces with the control segments indicated in the figure are effectively the controlled quantities.

Time traces of these quantities are shown in figure 4(*b*), showing that after some small oscillations during the ramp-up phase of the discharge, the controller is able to hold the inboard and secondary flux surfaces relatively fixed throughout the flattop. To simplify tuning, only proportional gain was typically used, as a result, a steady-state error between the requested and real-time calculated values persists during the discharge. This error could be driven to zero through the use of integral control if required. Also shown are the post-shot, fully-converged, magnetics-only EFIT (EFIT01) calculated flux surface locations, showing that while the secondary flux location is well-estimated by the real-time algorithm, the inboard flux position is offset from the EFIT01 calculated position. The main driver of the difference in EFIT01 and the position calculated by equation (5) is the assumption that the radial derivative of the flux is a constant along the control segment. Also, since the shot is diverted, the inboard flux surface position is offset from the plasma boundary location. The controller is able to achieve acceptable time response and keep these quantities steady throughout the flattop discharge. The offsets between actual and estimated flux surface positions are acceptable for the early and late parts of the discharge where the desired shape evolution is typically independent of the experiment, or for controlling highly-reproducible discharges, as the operator can empirically achieve desired outer gap sizes and elongations by adjusting the requested values from shot-to-shot during scenario development activities. However, the wide range of proposed scenarios and experiments on NSTX-U drives a requirement for more sophisticated shape control.

4. Real-time equilibrium reconstruction

To enable more precise control of the plasma shape during the main part of the discharge, a realistic solution to the plasma force balance is calculated in real-time, providing a better estimation of the position of the plasma boundary. The rtEFIT algorithm [45] was used for real-time equilibrium reconstruction for several years on NSTX, beginning in 2003 [27]. For NSTX-U, several updates and upgrades have been made to the algorithm, which are described in this section.

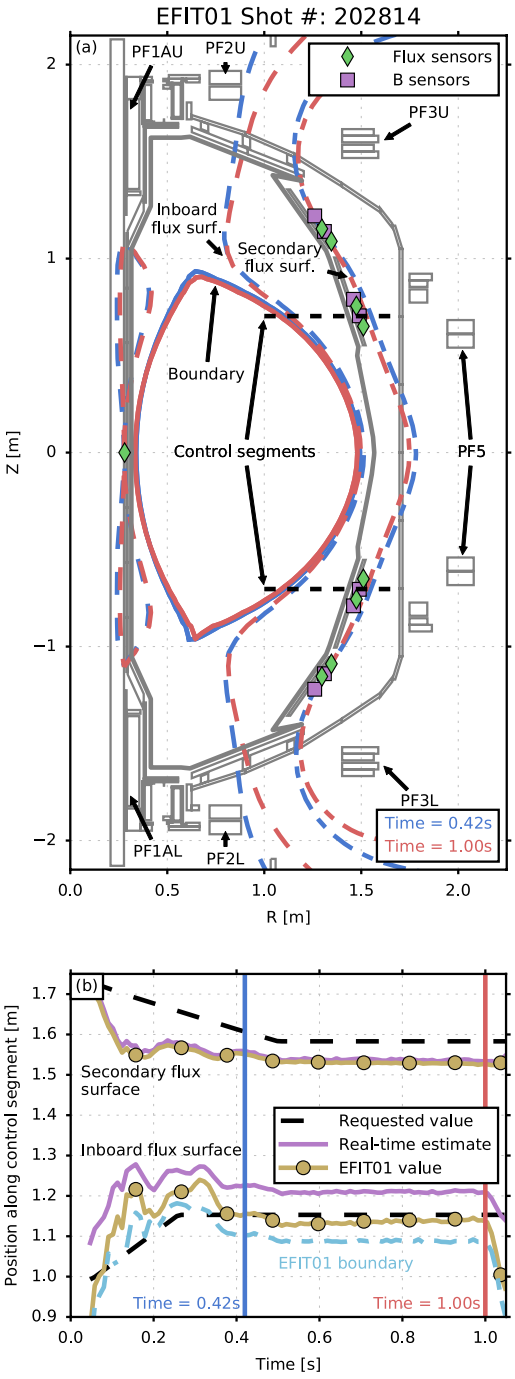

Figure 4. (*a*) Comparison of plasma boundaries (solid), inboard flux surfaces (dashed), and secondary flux surfaces (dash–dot) at $t = 0.42$ s and $t = 1.00$ s during shot 202 814, along with the flux sensors (green diamonds) used in the online calculation of intersections with control segments (black-dashed). (*b*) Time traces of the position along the control segments of the requested (black, dashed), online estimated (purple, solid), and offline EFIT01 estimated (gold, circles) inboard and secondary flux surfaces, along with the EFIT01 estimated plasma boundary (light blue, dash–dot).

4.1. Diagnostics and conductor modeling

First, the number of magnetic diagnostics on the machine was increased during the upgrade, and a majority of the new and existing measurements were made available to the real-time system [37]. Secondly, the model of active coils and conducting vessel structures used in the reconstruction was updated (new tables of Green's function values were calculated) to reflect the new center-stack and other changes made to the device during the upgrade. While the active coil currents typically dominate the externally produced field, the effects of vessel currents on the reconstruction can be significant in periods of high loop voltage and/or low plasma current, e.g. the ramp-up phase of the discharge. The finite elements of the vessel model were combined into thirty groups of elements, each associated with a loop voltage measurement, and the optimal 'effective resistances' were identified for each group based on vacuum magnetic diagnostic calibration shots for use in the measurement of vessel eddy currents in real-time as described in [47]. The spatial grid used to discretize the model of the plasma current was increased from 33×33 to 65×65, now matching the resolution of the standard offline EFIT code used for NSTX-U [48, 49]. This increase in resolution reduces the uncertainty in the computed plasma boundary, especially the X-point locations. The components of the plasma current model ($P'(\psi_N)$ and $FF'(\psi_N)$ where P is the plasma pressure, $F = 2\pi RB_t/\mu_0$ is related to the poloidal current, ψ_N is the flux normalized to the boundary flux, and prime denotes the derivative with respect to poloidal flux) were represented by polynomials with orders and constraints set to match the model used in the offline magnetics-only EFIT code. The parameterization has a total of four free parameters.

4.2. Performance improvement through multi-threading

The rtEFIT algorithm is split into a 'slow loop', which completes an iteration of the equilibrium reconstruction, and a 'fast loop' which updates the errors used by the shape controller on a 200 μs time scale based on the response matrix calculated in the last completed slow loop and the latest measurements (see [45] for details). PCS hardware and software improvements (including upgrading the computing infrastructure to use 64 2.8 GHz cores and upgrading compiler tools to take advantage of the newer hardware) enabled completion of the rtEFIT slow loop calculations with vessel current measurements treated as known values (zero uncertainty in fitting) at the new increased grid resolution to be as low as 3.4 ms. However, timing tests using processor-in-the-loop (PIL) simulations of the control system showed that the calculation time became unacceptably slow when treating the vessel currents as uncertain fitted parameters and calculating β_N, ℓ_i, and the q profile in real-time.

To overcome this limitation, the system was set up to make use of the multi-threading capabilities of rtEFIT and the remaining available cores on the real-time computer. In this mode, the rtEFIT calculations are split into three branches: a set of serialized data processing tasks (branch 0), and two independent branches (branch 1 for the equilibrium reconstruction and branch 2 for the calculation of β_N, ℓ_i, and the q profile) that can be run in parallel after completing the branch 0 tasks. Through the PCS user interface, the total number of threads allocated for rtEFIT, all of which are used for the branch 0 tasks, can be distributed to the parallel branches. A PIL simulation study was performed to assess the timing

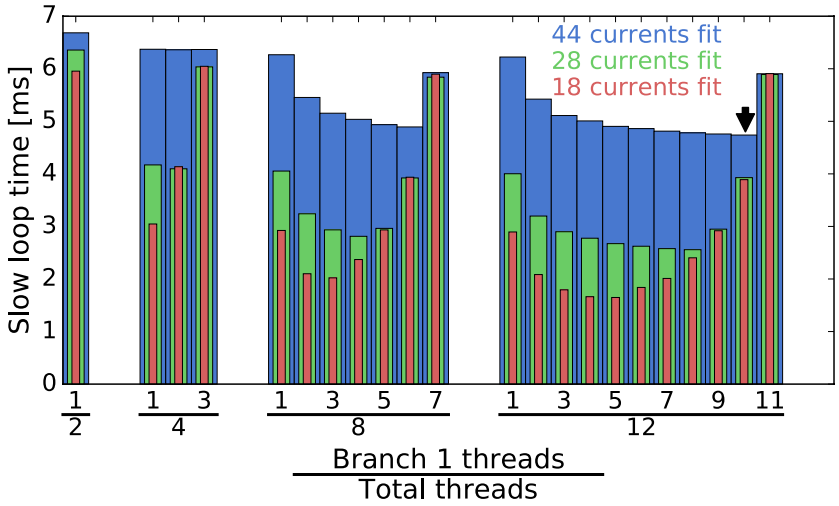

Figure 5. Slow loop time as a function of thread distribution and number of vessel currents fit. The optimal combination of threads for fitting all of the currents that are fit in the offline EFIT code (10 branch 1 threads and 2 branch 2 threads) is indicated with a black arrow.

benefits of increasing the total number of threads and to optimize the allocation of threads between the two branches. The results, displayed in figure 5, show that using 10 branch 1 threads and 2 branch 2 threads enables fitting 44 currents with a slow loop time <5 ms (indicated by black arrow). As the number of fitted currents is reduced, the optimal mix of threads shifts, favoring more branch 2 threads, and the slow loop time drops below 2 ms. The optimal time drops as the total number of threads increases, however the drop is less significant for larger numbers of fitted currents, indicating that improvements to the parallelization of the fitting procedure may be needed to keep the slow loop time small compared to the characteristic time of the vessel, which is around 10 ms.

A comparison of the reconstructed distance along the control segments used for shape control (described in the following section) resulting from the real-time EFIT (EFITRT) calculations with all vessel currents fit and an off-line magnetics-only fully converged EFIT (EFIT04[6]) is shown in figure 6. Very similar results are obtained for all four segments, with the largest errors occurring during transients during plasma current ramp-up ($t < 0.4$ s) and ramp-down ($t > 1.42$ s). During flattop, the deviation remains below 2 cm. Future software and hardware upgrades will aim to achieve faster slow loop computation time to enable multiple iterations per slow loop cycle while still fitting vessel currents, which should reduce discrepancies. Optimization of the discretization of the vessel model (to reduce the number of fitted currents while maintaining fidelity) will also be explored.

4.3. Filtering the effects of power supply ripple

While the measured signals entering the real-time system are sampled with a 200 μs data acquisition rate, the slow loop of rtEFIT runs at a reduced sample time and is therefore subject to corruption by under sampling high-frequency signals. On NSTX this effect did not cause problems with the reconstructions, however, it was observed on NSTX-U that the high frequency current ripple caused by the rectifiers for the the new lower-inductance PF1A coils was aliased into low frequency oscillations in the reconstruction. This aliasing effect, which is illustrated in figure 7, had only a small effect on the boundary reconstruction, however, it caused significant errors in the fit to the magnetic measurements and large oscillations in global quantities like β_N and l_i. Since future feedback control algorithms will make use of these calculated signals, it is important to improve the quality of their estimation.

To resolve the problem, a digital implementation of a multi-pole filter running on the fast (200 μs) sample rate was added to filter the measurements prior to their being sent to the CPU that does the slow loop calculation. A 2nd-order Butterworth filter with its cutoff frequency equal to half of the slow loop sampling frequency was found to effectively remove the oscillations due to aliasing and improve the overall fit to the magnetic measurements. The improvement in fitting and estimation of β_N on data from discharge 204 200 is shown in figure 8. The fitting quality is illustrated by $\chi^2 = \sum_i (D_i - C_i)^2/\sigma_i^2$ where the sum is over each of the diagnostics, D_i is the measured value for the ith diagnostic, C_i is the calculated value, and σ_i is the measurement uncertainty. Not only are the oscillations reduced when using the filter, but the overall fitting quality is improved (χ^2 is reduced). As an aside on fitting quality, these comparisons were done without fitting vessel or coil currents; χ^2 is typically reduced to between 100 and 200 by adding these additional degrees of freedom. This is comparable to the values obtained with the offline reconstruction. Though the filtering evidently greatly improves the quality of the reconstructions, it is also planned to reduce the magnitude of the current ripple in future campaigns with the addition of series inductors to the divertor coil circuits.

[6] The automatic post-shot fully converged magnetics-only EFIT run is referred to as EFIT01. EFIT04 is used for special runs, in this case activating the option to include a rigid vertical shift of the plasma in the fit. This option is not typically used in EFIT01 but its use is enforced in real-time EFIT.

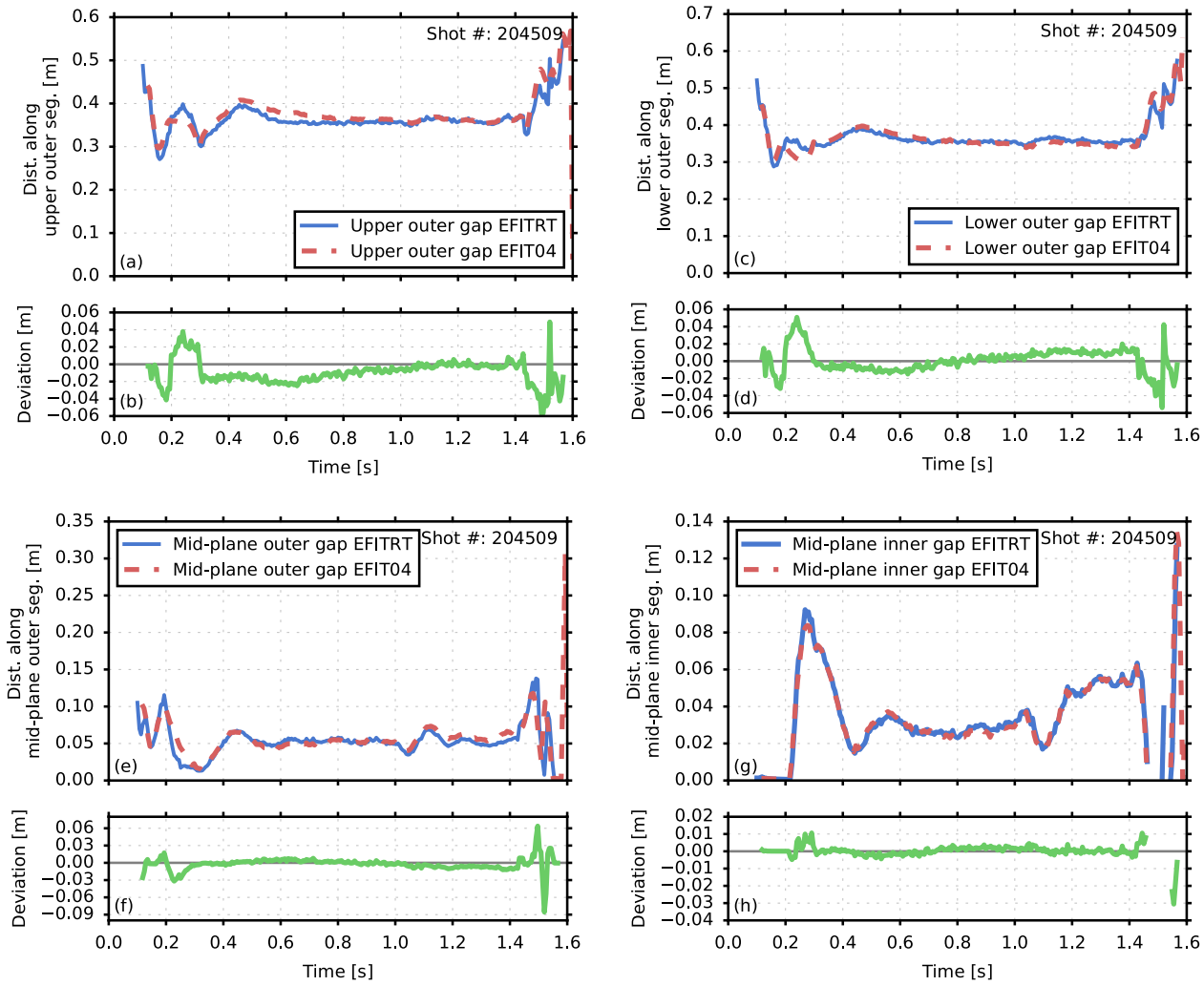

Figure 6. Comparison of the reconstructed distance along the control segments used for shape control for real-time EFIT, EFITRT (blue, solid), and off-line magnetics-only fully converged EFIT, EFIT04 (red, dashed), along with the deviation between the two reconstructions (green, solid).

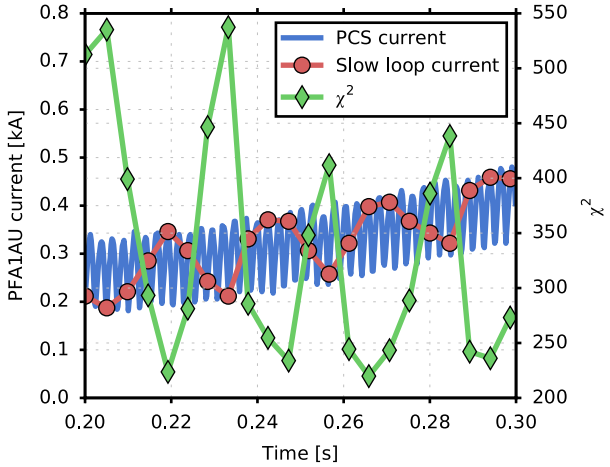

Figure 7. Low frequency oscillations in measurement fitting error χ^2 (red, diamond markers) clearly correlated with the low frequency oscillations of samples at the slow loop cycle times (black, circle markers) of the measured PF1AU coil current (blue, solid).

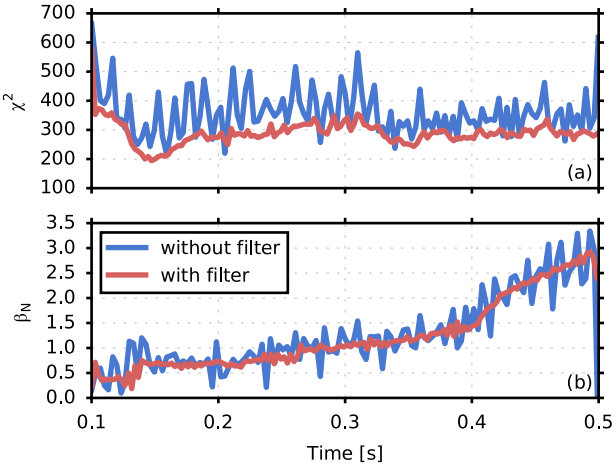

Figure 8. Comparison of the diagnostic fitting error (top) and the calculated value of β_N (bottom) for discharge 204 200 with the anti-aliasing filter off (red, circular markers) and the anti-aliasing filter on (blue, solid).

5. Isoflux shape control

This section describes the details of the isoflux algorithm calculations, updates for NSTX-U, and results of commissioning. In this algorithm, a vector, E, containing the errors for each of the controlled quantities (e.g. control point flux errors, X-point radial and vertical location errors), is formed. Each element E_i is low-pass filtered with a time constant $\tau_{\mathrm{LPF},i}$ to remove high-frequency noise, and the result is operated on by PID controllers with gains $k_{\mathrm{P},i}, k_{\mathrm{I},i}, k_{\mathrm{D},i}$ set individually for each quantity, resulting in a vector P:

$$P_i = \mathrm{PID}(\mathrm{LPF}(E_i, \tau_{\mathrm{LPF},i}), k_{\mathrm{P},i}, k_{\mathrm{I},i}, k_{\mathrm{D},i}). \quad (9)$$

The vector of voltage requests for each coil are calculated as

$$V_{\mathrm{isoflux}} = MP, \quad (10)$$

where M is a mixing matrix chosen to scale and distribute the P vector values to the appropriate coils in the form of power supply voltage requests. This allows flexible coil assignments: some coils can be assigned to be the sole coil responsible for controlling a single quantity, others can be assigned to respond to multiple quantities simultaneously, and others can be assigned to work together to control a particular quantity or set of quantities. The coil assignments typically used are described in the following subsections. For the results described in this section, the M matrix and PID gains were initially tuned in simulations using a a vacuum coil/vessel circuit model, i.e. only considering the dynamic response of flux to changes in coil and vessel currents, not changes due to the plasma. Gains were then fine tuned empirically during a small number of commissioning discharges to achieve the desired time response.

On NSTX, separate feedback algorithms were used to control inner-wall limited discharges and diverted discharges, with the latter enabling control of X-point and strike point locations [29, 30]. For NSTX-U, the code for both algorithms has been re-written to make use of the code generator capability included in the General Atomics supplied PCS software package [38]. The code generator uses the compiler's C pre-processor to generate header include files from a list of configuration parameters, allowing the developer to concentrate on algorithm functionality instead of interfacing with the underlying PCS framework. This reduces development time, improves maintainability and makes future upgrades easier to implement. As an example, the number of lines of code specific to the diverted plasma control algorithm was reduced by 75% while maintaining all original capabilities and adding several new ones.

5.1. Control of inner-wall limited shapes

The inner-wall limited algorithm, which adjusts the coil voltage requests to match the flux at the control points to the flux at the center-stack touch point, has been commissioned to use the PF3 upper and lower coils and the PF5 coils to control three points on the outer boundary of the plasma. In figure 9, the distances from the start of the control segment to the target and achieved boundary intersection point are compared for both the mid-plane outer gap and the lower outer gap for discharge 203 474. The results show that after some initial small oscillation, the boundary intersections remain very close to the the target locations (within 2–3 cm) throughout the discharge, slowly getting closer over time due to the integral term in the controller. The upper outer gap is not displayed because it has an identical target and nearly identical evolution during the discharge.

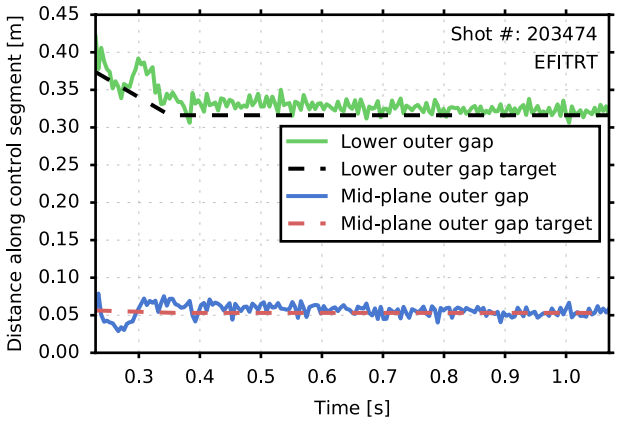

Figure 9. Tracking performance during a limited discharge showing the achieved (green, solid) and target (black-dashed) lower outer gap, as well as the achieved (blue, solid) and target (red-dashed) mid-plane outer gap for discharge 203 474.

5.2. Control of diverted shapes

To transition to a diverted discharge, the divertor coils are controlled to track a pre-programmed current trajectory to bring X-points into the vessel. The timing of the transition to the diverted shape control algorithm is selected prior to the discharge and is intended to occur when the shape is close to diverting. In the previous version of the diverted discharge algorithm, the PF3 coils and PF5 coils were used to control the flux at three points on the outer boundary of the plasma to match the flux at the dominant X-point. The algorithm has been modified to automatically switch to use the center-stack touch point as its reference point if the plasma is still limited when the operator programmed algorithm transition occurs, or if the plasma happens to limit during the shot. Prior to this modification, if the plasma happened to limit on the center-stack due to a disturbance or oscillation while using the diverted discharge isoflux algorithm, the controller still used the dominant X-point flux as its reference flux, which was no longer equivalent to the flux at the plasma boundary. This discrepancy in the reference flux resulted in the plasma boundary being pushed inboard, often causing the plasma to stay in a limited configuration throughout the remainder of the shot with the dominant X-point flux surface, instead of the actual plasma boundary, passing through the control points. This is illustrated in figure 10(*a*).

In shots with the modification to the selection of the active reference flux, like the one shown in figure 10(*b*), the boundary is controlled to pass through the control points as desired, even if the plasma happens to momentarily limit during an oscillation.

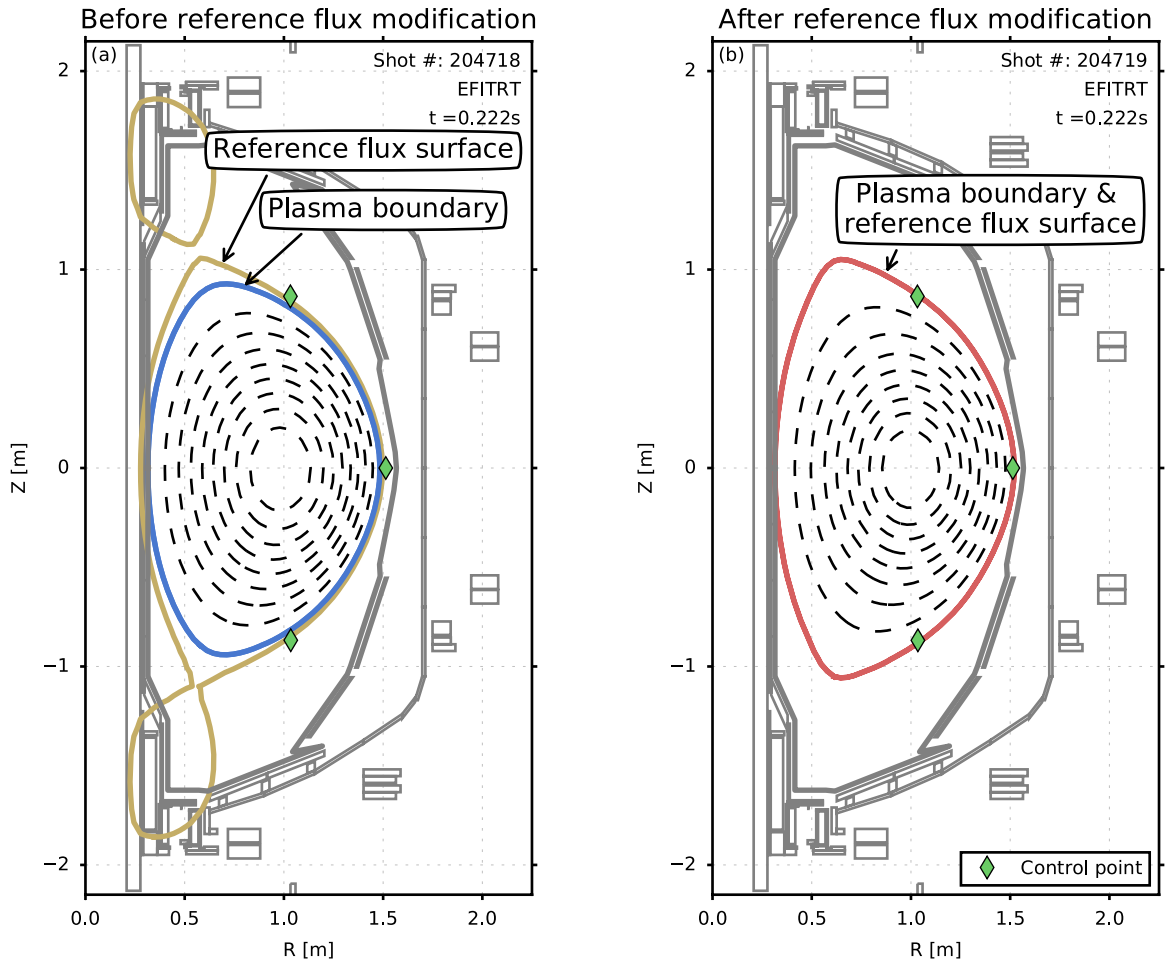

Figure 10. (*a*) Plasma boundary (blue), the flux surface defined by the dominant X-point flux (gold), and the outer gap control points at 0.22 s in discharge 204 718, in which the reference flux modification had not yet been implemented. (*b*) Plasma boundary (red) and outer gap control points at 0.215 s in discharge 204 719, which had the reference flux modification active.

5.3. Control of X-point and strike point locations

The PF1AU/L and PF2U/L coils have been commissioned to simultaneously control either the X-point radial and vertical positions or the X-point heights and the radius of the outer strike points. While the previous NSTX X-point and strike point control scheme linked each quantity to a single divertor coil [30], the X-point and strike point control for NSTX-U is multi-input-multi-output (MIMO), accounting for the interaction of the coils in the control law. The MIMO control law was obtained by calculating the Jacobian matrix relating changes in coil currents to changes in X-point and strike point locations for a particular target equilibrium, and finding the weighted pseudo-inverse of this matrix. Weights were chosen according to which quantities were to be controlled for a particular shot (the combinations of X-point radial and vertical position as well as X-point vertical position and outer strike point radial position were considered during this campaign). The pseudo-inverse matrix, which indicates the optimal 'direction' for changing coil currents in response to X-point location and strike point flux errors, was entered into the appropriate elements of the isoflux algorithm's M matrix, while PID gains for the respective error quantities were chosen, as described before, based on simulations of the coil/vessel circuit model and fine tuned empirically during commissioning discharges. In figure 11, successful tracking of the X-point radial and vertical position during the diverted discharge 204 602 is shown.

Use of the feedback controller to track a series of step changes in the requested outer strike point positions during a single shot (203 879) is illustrated in figure 12. The controller was able to track the requests at each step, while keeping the X-point heights and the outer boundary locations fixed. Carbon II emission on the lower divertor during the shot is shown in figure 13, along with the target and reconstructed strike-point positions. Visible emission from the lower divertor is measured using one of the two 2D wide angle fast cameras aimed at the lower divertor and filtered via a narrow-bandpass interference filter [50]. In attached divertor conditions, such as those in the discharge presented in this paper, C II emission (514 nm) is localized at the surface of the plasma facing components (its emission shell being representative of plasma at a few eVs). Spatial calibration is performed using in-vessel metrology via a mechanical arm and the simultaneous unfiltered imaging of the lower divertor plasma facing components with in-vessel illumination. The reconstructed strike point position is well aligned with the peak of the emission, and the time response

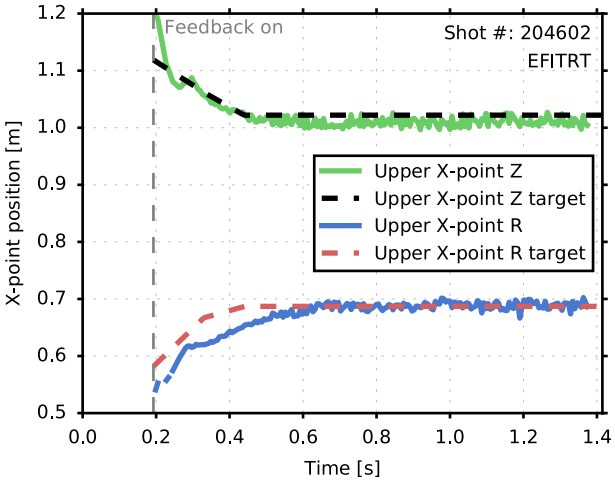

Figure 11. X-point position tracking performance during a diverted discharge showing the target (black, dashed) and achieved (green, solid) upper X-point *Z* position, as well as the target (red, dashed) and achieved (blue, solid) upper X-point R position for discharge 204 602.

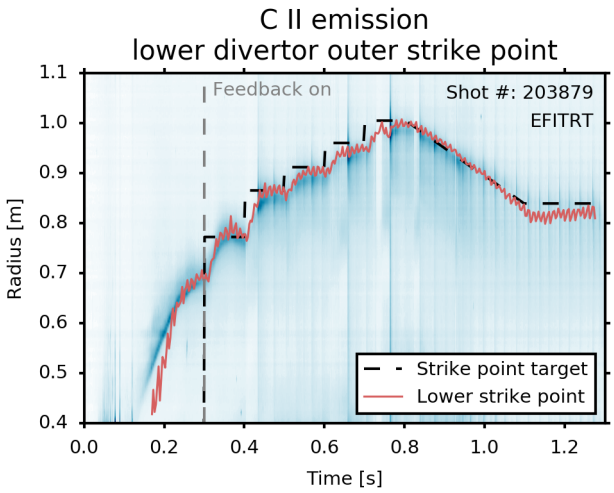

Figure 13. Carbon II emission on the lower divertor during shot 203 879 over-layed with the target strike point location (black, dashed), showing that the EFITRT estimated strike point position (red, solid) is well aligned with the peak of the emission and tracks the target after feedback is turned on.

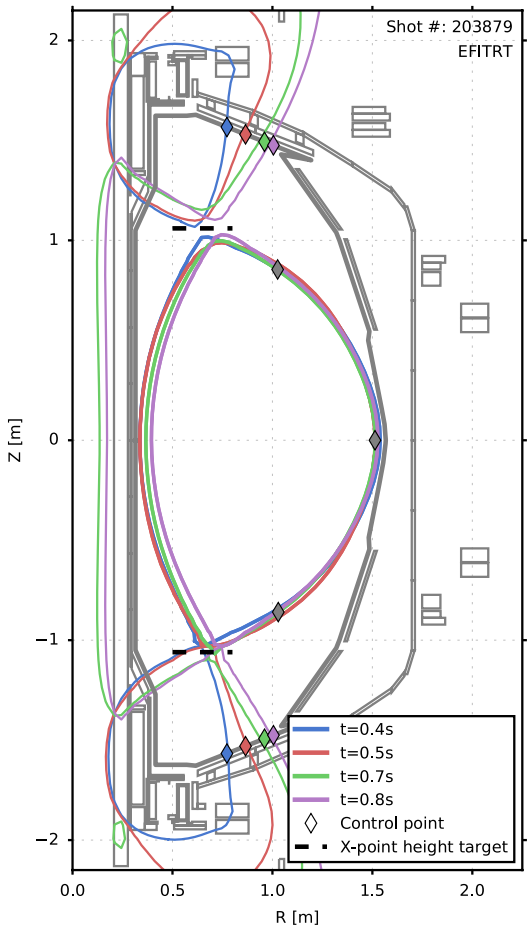

Figure 12. Plasma boundary at various times 203 879 showing tracking of the strike point targets (colored diamonds on outboard divertor) while maintaining the outer gap targets (red diamonds) and the height of the X-points (dashed black lines).

to changes in target location is very good, especially at larger strike point radii (>0.9 m). There is some overshoot at smaller radii, likely indicating that the plasma response to the divertor coils changes appreciably over the range of radii considered. This motivates future research into upgrading the algorithm to automatically update the M matrix and PID gains in response to changes in the X-point and strike point targets.

5.4. Control of δr_{sep}

To actively maintain balanced double null, as well as lower-, and upper-biased discharges, feedback control of the parameter δr_{sep} has also been commissioned. This parameter is defined as the horizontal distance between the two flux surfaces that are defined by the upper and lower X-points as measured at the outboard mid-plane plasma boundary. Figure 14 shows a series of equilibria from a feedback controlled scan in which the target value of δr_{sep} was varied to achieve (a) an upper-biased shape ($\delta r_{sep} > 0$), (b) a balanced double null shape ($\delta r_{sep} = 0$), and (c) a lower-biased shape ($\delta r_{sep} < 0$). Time traces comparing the target and achieved δr_{sep} during these shots are shown in figure 15.

The δr_{sep} control method has been updated from that used previously on NSTX [27] to adjust the location of the boundary control point targets in real-time based on the measured δr_{sep} tracking error in order to appropriately bias the up-down symmetric target shape to track the requested δr_{sep}. The measured value of δr_{sep} is calculated in real-time as

$$\delta r_{sep} = (\psi_{x,1} - \psi_{x,2}) / G_{mp}, \tag{11}$$

where $\psi_{x,1}$ is the flux at the lower x-point, $\psi_{x,2}$ is the flux at the upper x-point, and G_{mp} is the radial flux gradient at the outboard mid-plane control point. The tracking error $E_{sym} = \delta r_{sep} - \delta r_{sep,req}$ is then operated on with a PID controller to produce the value P_{sym}, i.e.

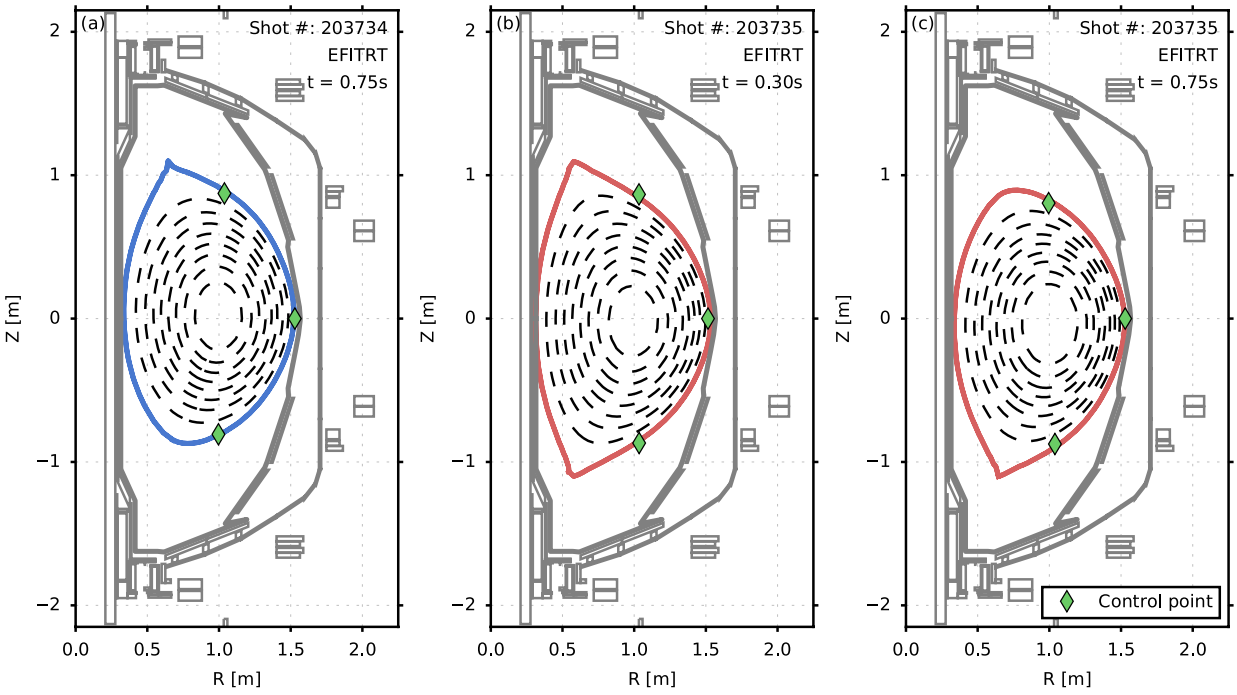

Figure 14. A series of three equilibria (*a*) 203 734, $t = 0.75$ s, (*b*) 203 735, $t = 0.3$ s, (*c*) 203 735, $t = 0.75$ s, from two discharges in which the target for δr_{sep} was ramped from 0 cm to ± 1 cm during the discharge. The target boundary locations are shown as green diamonds.

$$P_{\text{sym}} = \text{PID}(\text{LPF}(E_{\text{sym}}, \tau_{\text{LPF,sym}}), k_{\text{P,sym}}, k_{\text{I,isym}}, k_{\text{D,sym}}), \quad (12)$$

where $\tau_{\text{LPF,sym}}$ is the time constant for a low-pass filter used to remove high-frequency noise, and the PID gains are $k_{\text{P,sym}}, k_{\text{I,sym}}, k_{\text{D,sym}}$. Based on this result, the location of the control point associated with each control segment is adjusted, modifying the symmetry of the boundary shape such that E_{sym} is reduced. For the ith control segment, the adjustment a_i, in meters along the segment, is calculated as

$$a_i = (G_{mp}/G_i)\left(s_{t,i}\delta r_{\text{sep,req}} f_i + s_{\text{PID},i} K_i P_{\text{sym}}\right), \quad (13)$$

where G_i is the flux gradient along the ith control segment at the ith control point, K_i is the weight on the feedback term for the ith control segment, f_i is the weight on the feedforward adjustment for the ith control segment. The terms $s_{t,i}$ and $s_{\text{PID},i}$ are signs and weights that change depending on the sign of δr_{sep}: for lower biased shapes, only the segments in the upper half of the device are adjusted with a weight of 1, for upper biased shaped, only the segments in the lower half of the device are adjusted with a weight of 1, and for balanced shapes, all segments are adjusted with the weight reduced to 0.5. For NSTX-U, only the upper and lower outer boundary segments (which are associated with PF3U/L) are set up to be adjusted by this algorithm.

The new control approach is in contrast to the older method in which the target shape was biased by a feedforward adjustment and the δr_{sep} tracking error was used to augment the PF3 voltage request directly. The older method resulted in inconsistencies between the target shape and the shape needed to achieve δr_{sep} target that made feedback loop tuning and interpretation of results more complex.

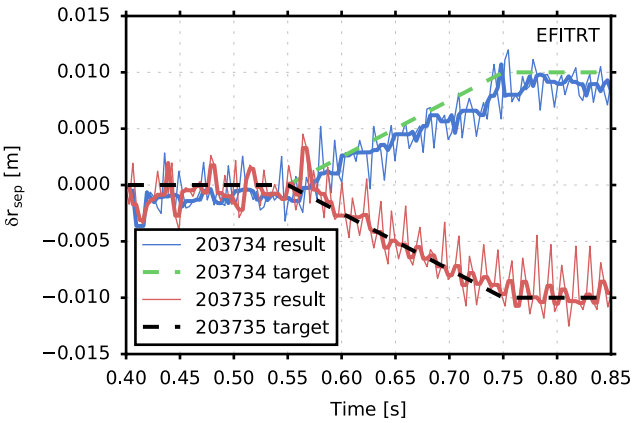

Figure 15. Comparison of the achieved (solid) and target (dashed) δr_{sep} in shots 203 734 (blue) and 203 735 (red). The thicker solid lines are the achieved values with a 5 sample median filter applied to remove the oscillations in the reconstruction caused by aliasing of divertor coil current ripple (these shots preceded the introduction of the anti-aliasing filters described in section 4).

5.5. Control of mid-plane inner gap size

A new method for controlling the inner gap (the mid-plane gap between the plasma boundary and the center-stack) has also been commissioned for NSTX-U. Inner gap control on a spherical torus is challenging because there are no shaping coils on the in-board mid-plane of the machine. Furthermore, each of the active shaping coils currently in use on NSTX-U have been assigned to controlling points on the outboard side of the machine, or to controlling the X-point or strike-positions, meaning the inner gap cannot be independently controlled. One approach to inner gap control would be to adjust

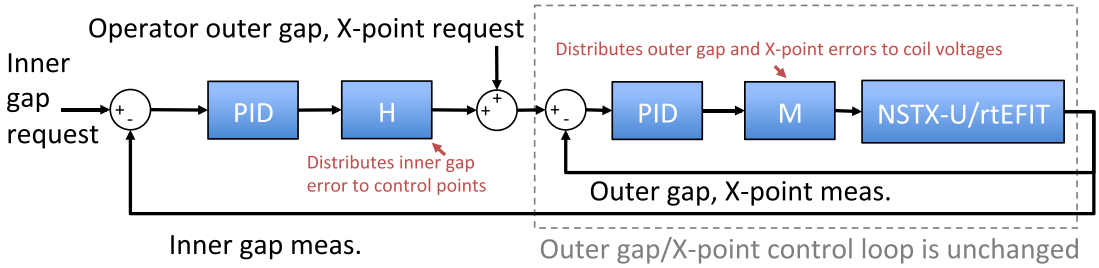

Figure 16. Schematic of isoflux modifications to isoflux shape controller for inner gap control showing how the outer gap and X-point requests are adjusted based on the inner gap error.

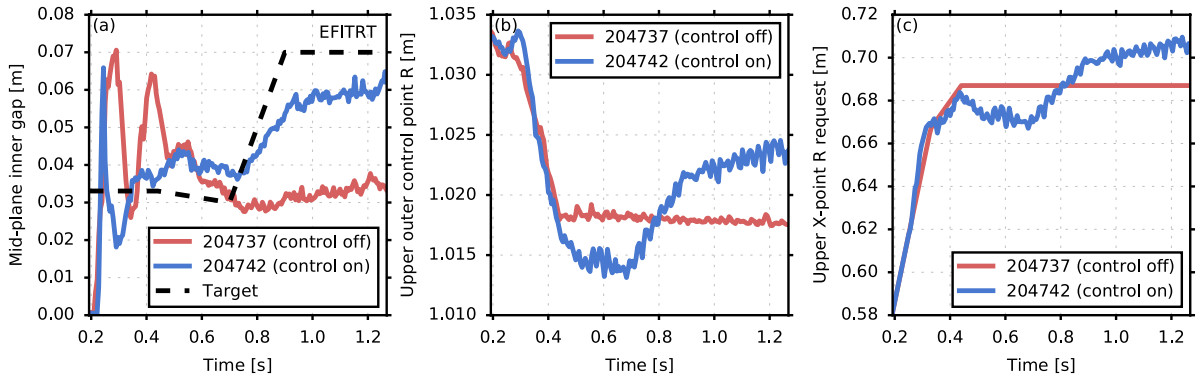

Figure 17. (*a*) Achieved (blue) and target (red, dashed) inner gap in discharge 204 742. X-point radial target (*b*) and radial position of the upper-outer-squareness control point (*c*) showing the feedback modified targets in 204 742 compared to those with inner gap control off in 204 737.

the matrix M to weight the inner gap error in one or more coils, in addition to the weight on the gaps or X-point locations already assigned to the respective coils. However, since this would require retuning the control loops for the outer gaps and X-point locations, and the active control of the inner gap was only found to be necessary after commissioning of the other control loops had been completed, an alternative approach was implemented. In the approach taken, target locations of each control point along with the X-point radial and vertical target locations are modified away from the pre-programmed values in real-time to improve tracking of the inner gap target. This scheme, illustrated in figure 16, allows the operator to easily chose from shot to shot how the target plasma shape should change in real-time to improve tracking of the inner gap target (mimicking/automating the shape target development process previously done shot-to-shot by operators) without requiring modification of the established control gains for outer gap and X-point control.

The flux error at the target location of the mid-plane inner plasma boundary is operated on by a PID operator to form P_{inner}. This flux error is then used to calculate an adjustment to the ith control point $a_{\text{inner},i}$ based on a weight for the ith control point H_i, i.e.

$$a_{\text{inner},i} = P_{\text{inner}} H_i / G_{\text{inner}}, \tag{14}$$

where G_{inner} is the radial flux gradient at the inner gap target location, which is used to convert the flux error to a positional error.

Figure 17(*a*) compares the achieved and requested inner gap in shot 204 742, in which the requested inner gap was ramped from around 3 cm to 7 cm between 0.7 s and 0.9 s. Because the integral gain was small in this example, a steady state error persists throughout the shot, however, it is clear that the controller is able to modify the gap with good time response. The modifications prescribed by the feedback controller for the target X-point radial position and the radial position of the control point on the upper outer control segment are shown in figures 17(*b*) and (*c*), respectively. The corresponding values in the reference shot 204 737, which did not have inner gap control activated, are shown for comparison. In the closed-loop shot, the inner gap control algorithm moved the X-point and control point locations slightly inboard to decrease the inner gap, then ramped to larger radii to increase the outer gap. The necessary modifications were small, on the order of the requested change in inner gap. This new capability will enable improved reproducibility of the inner gap evolution during the ramp-up phase of discharges, which was found to be critical for achieving reliable H-mode access [3].

6. Conclusion

Rapid progress has been made in commissioning the upgrades to the NSTX-U control system, including the important areas of real-time reconstruction and boundary shape control. The plasma shape control algorithms have been updated and tuned for the new device, enabling accurate reproducible control of the plasma boundary locations during all phases of the discharge. A flux projection gap control algorithm has been established for early in the discharge as well as during the ramp-down phases of the discharge, enabling outer gap and elongation control when real-time reconstructions are

unreliable. During the main part of discharges, real-time reconstructions are used to produce flux and position errors for the ISOFLUX control scheme to act upon. The resolution of the real-time equilibrium reconstructions has been improved from what was used in NSTX to match that of the offline reconstruction code, fitting of the coil and vessel currents in real-time has been activated, and measurement filtering has been added to improve reconstruction quality. ISOFLUX control of the boundary locations and δr_{sep} has been demonstrated, and the ability to automatically switch the reference flux used in determining flux errors when the plasma transitions from limited to diverted configurations has been added. This new capability improves boundary control near the time of diverting. MIMO control of the X-point and strike point locations was demonstrated, and a new MIMO approach to controlling the mid-plane inner gap in real-time, a challenge for spherical torus devices, has been implemented and tested. These tools have been critical to the early commissioning activities on NSTX-U, especially for the development of L-mode and H-mode scenarios, and will be used to enable careful scans of shaping parameters during future campaigns.

Next steps for real-time reconstruction on NSTX-U will involve adding motional Stark effect (MSE) and Thomson scattering constraints, which will improve the estimation of internal profiles, and working to improve parallelization of the reconstruction algorithm to enable multiple iterations. Next steps for real-time control include commissioning feedback control algorithms for the plasma stored energy, current profile, rotation profile, and the 'snowflake' divertor configuration. The use of a fully multi-input-multi-output control scheme that accounts for the interaction of the coils on all controlled quantities will also be explored [51].

Acknowledgments

This work was supported by the US Department of Energy Grant under contract number DE-AC02-09CH11466.

Notes: The digital data for this publication can be found in: http://arks.princeton.edu/ark:/88435/dsp018623j140r

Notice: This manuscript is based upon work supported by the U.S. Department of Energy, Office of Science, Office of Fusion Energy Sciences, and has been authored by Princeton University under Contract Number DE-AC02-09CH11466 with the U.S. Department of Energy. The publisher, by accepting the article for publication acknowledges, that the United States Government retains a non-exclusive, paid-up, irrevocable, world-wide license to publish or reproduce the published form of this manuscript, or allow others to do so, for United States Government purposes.

ORCID iDs

M.D. Boyer https://orcid.org/0000-0002-6845-9155
D.J. Battaglia https://orcid.org/0000-0001-8897-9740
N. Eidietis https://orcid.org/0000-0003-0167-5053
J. Menard https://orcid.org/0000-0003-1292-3286
C.E. Myers https://orcid.org/0000-0003-4539-8406

References

[1] Menard J. *et al* 2012 *Nucl. Fusion* **52** 083015
[2] Menard J.E. *et al* 2017 *Nucl. Fusion* **57** 102006
[3] Battaglia *et al* 2018 *Nucl. Fusion* (https://doi.org/10.1088/1741-4326/aaa6e0)
[4] Ono M. *et al* 2000 *Nucl. Fusion* **40** 557
[5] Sykes A. *et al* 2001 *Nucl. Fusion* **41** 1423
[6] Goldston R. *et al* 2008 An experiment to tame the plasma material interface FT/P3-12 *Proc. 22nd Int. Conf. on Fusion Energy (Geneva, Switzerland)* (IAEA)
[7] Stambaugh R.D. *et al* 2010 Candidates for a fusion nuclear science facility (FDF and ST-CTF) P2.110 *37th EPS Conf. on Plasma Physics (Dublin, Ireland) vol* 51
[8] Menard J.E. *et al* 2016 *Nucl. Fusion* **56** 106023
[9] Menard J. *et al* 2011 *Nucl. Fusion* **51** 103014
[10] Kaye S. *et al* 2015 *Nucl. Fusion* **55** 104002
[11] Kaye S. *et al* 2006 *Nucl. Fusion* **46** 848
[12] Kaye S. *et al* 2007 *Phys. Rev. Lett.* **98** 175002
[13] Kaye S. *et al* 2007 *Nucl. Fusion* **47** 499
[14] Valovic M. *et al* 2011 *Nucl. Fusion* **51** 073045
[15] Fredrickson E.D. *et al* 2006 *Phys. Plasmas* **13** 056109
[16] Gryaznevich M. *et al* 2008 *Nucl. Fusion* **48** 084003
[17] Podesta M. *et al* 2009 *Phys. Plasmas* **16** 056104
[18] Fredrickson E.D. *et al* 2009 *Phys. Plasmas* **16** 122505
[19] Gates D. *et al* 2007 *Nucl. Fusion* **47** 1376
[20] Menard J. *et al* 2007 *Nucl. Fusion* **47** S645
[21] Gates D. *et al* 2009 *Nucl. Fusion* **49** 104016
[22] Gerhardt S. *et al* 2011 *Nucl. Fusion* **51** 073031
[23] Buttery R. *et al* 2004 *Nucl. Fusion* **44** 1027
[24] Chapman I. *et al* 2011 *Nucl. Fusion* **51** 073040
[25] Woolley R.D., Titus P.H., Neumeyer C. and Hatcher R.E. 2011 Digital coil protection system algorithms for the NSTX centerstack upgrade *Proc. IEEE/NPSS 24th Symp. on Fusion Engineering (Chicago, IL, USA)* (IEEE)
[26] Erickson K.G., Tchilinguirian G.J., Hatcher R.E. and Davis W.M. 2014 *IEEE Trans. Plasma Sci.* **42** 1811
[27] Gates D. *et al* 2006 *Nucl. Fusion* **46** 17
[28] Gerhardt S. *et al* 2010 *Fusion Sci. Technol.* **61** 11
[29] Kolemen E. *et al* 2010 *Nucl. Fusion* **50** 105010
[30] Kolemen E. *et al* 2011 *Nucl. Fusion* **51** 113024
[31] Boyer M. *et al* 2017 *Nucl. Fusion* **57** 066017
[32] Goumiri I.R. *et al* 2017 *Phys. Plasmas* **24** 056101
[33] Ilhan Z.O., Wehner W.P. and Schuster E. 2016 Model predictive control with integral action for the rotational transform profile tracking in NSTX-U *Proc. IEEE Conf. on Control Applications (Buenos Aires, Argentina)* (IEEE)
[34] Goumiri I. *et al* 2016 *Nucl. Fusion* **56** 036023
[35] Boyer M. *et al* 2015 *Nucl. Fusion* **55** 053033
[36] Berkery J.W., Sabbagh S.A., Bell R.E., Gerhardt S.P. and LeBlanc B.P. 2017 *Phys. Plasmas* **24** 056103
[37] Gerhardt S.P. *et al* 2014 *Rev. Sci. Instrum.* **85** 2012
[38] Erickson K. *et al* 2014 *Fusion Eng. Des.* **89** 853
[39] Gates D. *et al* 2006 *Fusion Eng. Des.* **81** 1911
[40] Ferron J.R., Penaflor B., Walker M.L., Moller J. and Butner D. 1995 A flexible software architecture for tokamak discharge control systems *Proc. of 16th Int. Symp. on Fusion Engineering* vol 2 pp 870–3
[41] Penaflor B.G. *et al* 2013 Latest advancements in diii-d plasma control software and hardware *IEEE 25th Symp. on Fusion Engineering* pp 1–4
[42] Meyer H. *et al* 2005 *Plasma Phys. Control. Fusion* **47** 843

[43] Maingi R. *et al* 2010 *Nucl. Fusion* **50** 064010
[44] Battaglia D. *et al* 2013 *Nucl. Fusion* **53** 113032
[45] Ferron J. *et al* 1998 *Nucl. fusion* **38** 1055
[46] Hofmann F. 1990 *Nucl. Fusion* **30** 2013
[47] Gates D.A., Menard J.E. and Marsala R.J. 2004 *Rev. Sci. Instrum.* **75** 5090
[48] Sabbagh S. *et al* 2006 *Nucl. Fusion* **46** 635
[49] Sabbagh S. *et al* 2001 *Nucl. Fusion* **41** 1601
[50] Scotti F., Roquemore A.L. and Soukhanovskii V.A. 2012 *Rev. Sci. Instrum.* **83** 3
[51] Shi W., Barton J., Alsarheed M. and Schuster E. 2011 Multivariable multi-modelbased magnetic control system for the current ramp-up phase in the National Spherical Torus eXperiment (NSTX) *50th IEEE Conf. on Decision and Control and European Control Conf. (Orlando, FL, USA) (*IEEE) pp 235–54